

Spectroscopy with Polarization Controlled Entangled Photons for Detecting Orbital Excitation in Solids

P.Munkhbaatar,* D.Ulam-Orgikh, and J.Vanchinkhuu

Department of Physics, School of Science, NUM, Ulaanbaatar 210646, Mongolia

We propose an excitation-probe measurement method utilizing entangled photon pulses. The excitation-probe signal is dominated by stimulated Raman scattering as well as two-photon absorption when the time delay between the excitation pulse and the probe pulse is shorter than the pulse duration. This paper demonstrates that the two-photon-absorption signal can be suppressed when the photons of the pulses are entangled. The stimulated Raman scattering signal can be composed of many peaks distributed over broad photon energies owing to the transitions between numerous quantum states in complex materials. We also show that the desired peaks among the many peaks can be selected by controlling the thickness of the nonlinear crystal, the pump pulse center frequency, and the polarization of the excitation pulse and probe pulse.

PACS numbers: 42.65.Lm, 78.47.J-, 78.47.D-

I. INTRODUCTION

The excitation-probe (or pump-probe) measurement technique is a useful tool to investigate the time dependence of excitations between quantum states of matter[1, 2]. The excitation pulse excites electric charges to high-energy states, thereby inducing nonlinear polarization in the sample material. The induced polarization yields emission of photon fields carrying the information of the electronic structure change or the quasi-particle excitation. Part of the probe pulse interferes with the emitted photons, producing measurable change in the intensity and phase of the probe pulse itself[3].

During measurement, the excitation and probe pulses together invoke complicated nonlinear processes. The dominant processes are usually stimulated Raman scattering (SRS) and two-photon absorption (TPA). The information available from the SRS process is of interest in many research areas including biological imaging and solid state spectroscopy[4–6]. However, it is difficult to separate the TPA signal from the SRS signal in typical excitation-probe measurement systems. Some techniques have been invented to discriminate the SRS and TPA signals[7, 8]. The quest for different techniques is still demanding.

The excitation-probe measurements are performed with two optical modes with wave vectors k_1 and k_2 and frequencies ω_1 and ω_2 in the simplest description. Suppose (k_1, ω_1) is the excitation mode and (k_2, ω_2) is the probe mode. Typical measurement detects the intensity change of the (k_2, ω_2) mode resulting from the cooperation of the eight quantum pathways invoked by the (k_1, ω_1) mode. The pathways are divided into the TPA group and the SRS

group[9]. All the pathways in the TPA group contain optical correlation functions of the form $\langle a^\dagger a^\dagger a a \rangle$; here, $a(a^\dagger)$ is the annihilation (creation) operator of the optical modes. The possible optical correlation functions for the TPA pathways are $\langle a_2^\dagger a_1^\dagger a_1 a_2 \rangle$, $\langle a_2^\dagger a_1^\dagger a_2 a_1 \rangle$, $\langle a_1^\dagger a_2^\dagger a_2 a_1 \rangle$, and $\langle a_1^\dagger a_2^\dagger a_1 a_2 \rangle$. The optical correlation functions of the SRS group are $\langle a_2^\dagger a_2 a_1^\dagger a_1 \rangle$, $\langle a_2^\dagger a_1 a_1^\dagger a_2 \rangle$, $\langle a_1^\dagger a_1 a_2^\dagger a_2 \rangle$, and $\langle a_1^\dagger a_2 a_2^\dagger a_1 \rangle$. For the classical optical modes, the intensity change due to all of the eight correlation functions become identical: $\langle a_2^\dagger \rangle \langle a_1^\dagger \rangle \langle a_2 \rangle \langle a_1 \rangle \sim |E_1|^2 |E_2|^2$ [9, 10]. This is the reason why the conventional excitation-probe method can hardly discriminate the TPA and SRS signals. However, if the quantum mechanical nature of the optical modes is harnessed, the intensity change due to TPA and SRS can be distinguished.

In this paper, we propose a method to suppress the contribution of TPA to the excitation-probe signal by controlling the quantum states of the excitation and probe pulses. We have applied the proposed method to simulate the excitation-probe signal of a model material system and demonstrate here in that the proposed method can suppress the TPA signal and select the SRS signal specifically.

II. THEORY

Figure 1a shows the proposed measurement setup. Here the photon pairs can be produced in pulsed mode by means of spontaneous parametric down-conversion (SPDC). A type-I nonlinear crystal is pumped by a Gaussian pulse with temporal duration T_1 and central frequency ω_p . The pulsed photon pairs can be described by a nonseparable wave function $|\Psi\rangle$ [11]:

$$|\Psi\rangle = \sum_{i,j} \Phi_{ij} b_{1i} b_{2j} |0\rangle, \quad (1)$$

*Electronic address: p_munhbaatar@yahoo.com

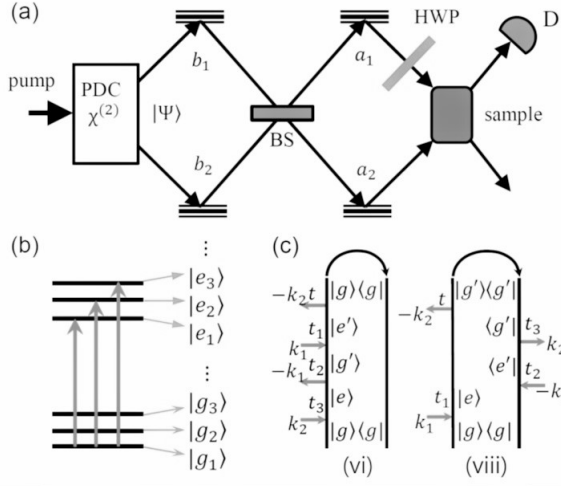


FIG. 1: (a) Proposed excitation-probe setup, (b) schematic structure of energy eigenstates of the model material system, and (c) closed-time path-loop diagrams for (vi) and (viii) pathways.

$$\Phi_{ij} = C \exp[-T_1^2(\omega_p - \omega_{1i} - \omega_{2j})^2] \text{sinc}[T_2(\omega_{2j} - \omega_{1i})]. \quad (2)$$

where T_2 is the entanglement time, defined by the difference between the inverse group velocities of the two photons. T_2 can be controlled by changing the thickness of the SPDC crystal. Fock state $b_1^\dagger b_2^\dagger |0\rangle$ has one photon in each mode k_1 and k_2 . C is proportional to the nonlinearity of the SPDC crystal and the pump electric field amplitude ε_{ex} [12].

Inspired by the work of Roslyak et al., I included an interferometer to control the quantum states of pulsed photon pairs[9]. The two photon modes (k_1, ω_1) and (k_2, ω_2) produced in the nonlinear crystal are directed into the input port of the broadband 50/50 beam splitter, which mixes the photon fields. The photons leaving the beam splitter can be described by a_1 for the excitation photon field and a_2 for the probe photon field[13]:

$$a_1 = 1/\sqrt{2}(-b_1 + Ib_2), \quad a_2 = 1/\sqrt{2}(Ib_1 - b_2). \quad (3)$$

We assumed that the excitation-probe signal is composed of eight pathway contributions[3, 9]. When the proposed setup is used, the following six photon correlation functions among the eight functions are all equal to zero:

$$\begin{aligned} \langle a_1^\dagger a_2^\dagger a_2 a_1 \rangle &= \langle a_1^\dagger a_2^\dagger a_1 a_2 \rangle = \langle a_2^\dagger a_1^\dagger a_2 a_1 \rangle = \\ \langle a_2^\dagger a_1^\dagger a_1 a_2 \rangle &= \langle a_1^\dagger a_1 a_2^\dagger a_2 \rangle = \langle a_2^\dagger a_2 a_1^\dagger a_1 \rangle = 0. \end{aligned} \quad (4)$$

Calculations of these functions are given in appendix A. Nonzero contributions thus arise only from the

other two pathways; $\langle a_2^\dagger a_1 a_1^\dagger a_2 \rangle$ of the (vi) pathway and $\langle a_1^\dagger a_2 a_2^\dagger a_1 \rangle$ of the (viii) pathway.

We considered crystalline LaMnO₃ as the model material system. To mimic one lattice layer of the orbital- and spin-ordered LaMnO₃ crystal, I built a Hamiltonian for an ideal Mn cluster composed of four Mn³⁺ ions. Details of the model material system and the Hamiltonian can be found in Ref.[14].

Figure 1b schematically illustrates the structure of the material systems energy eigenstates. $|g\rangle$ represents a set of eigenstates, i.e. $\{|g_1\rangle, |g_2\rangle, \dots\}$; $|g_1\rangle$ is the ground state. The energy difference between $|g_n\rangle$ and $|g_{(n+1)}\rangle$ arises from the phonon-orbital coupling energy difference for the different octahedral distortion and orbital ordering configuration. The second set, $|e\rangle = \{|e_1\rangle, |e_2\rangle, \dots\}$, represents the set of photoexcited eigenstates. The excited state corresponds to one hole and one double-occupied state. The energy difference between $|e_n\rangle$ and $|e_{(n+1)}\rangle$ arises from phonon-orbital coupling between the sites, similar as in $\{|g_n\rangle\}$. The energy difference between $|g_n\rangle$ and $|e_n\rangle$ arises mainly from Coulomb energy (U), since U is about 10 times the phonon-orbital coupling energy. The third set of higher-energy ($2U$) photoexcited states, $|f\rangle$ (not shown in Fig. 1a), are also considered in the interaction process. The values of U , J , Q_3 , q , and ω_{ph} used in the calculations were $5t$, $0.06t$, $0.27t$, $0.07t$, and $0.2t$, respectively. t is the hopping integral parameter representing the kinetic energy gain of the Mn ion electrons[14].

In the proposed excitation-probe setup, the probe signal is determined solely by the (vi) and (viii) pathways; loop diagrams for these pathways are given in Fig. 1c. In the (vi) pathway, the system evolves from the ground state ($|g\rangle$) to an excited state ($|e\rangle$) by absorbing a photon, then to a low-energy state ($|g'\rangle$) by emitting a photon. Then it assumes another excited state ($|e'\rangle$) by absorbing a photon, then finally returns to the ground state ($|g\rangle$) by emitting a photon. In the (viii) pathway, the system undergoes evolution from the ground state ($|g\rangle$) to an excited state ($|e\rangle$) by absorbing a photon, then to a low-energy state ($|g'\rangle$) by emitting a photon; then, the same process is repeated once in the bra-vectors.

The frequency-resolved signal, $S(\omega_1, \omega_2)$, is given by the following equation [3]:

$$\begin{aligned} S(\omega_1, \omega_2) &\sim \text{Im}[\chi^{(vi)}(\omega_1, \omega_2)] \langle a_2^\dagger a_1 a_1^\dagger a_2 \rangle \\ &+ \text{Im}[\chi^{(viii)}(\omega_1, \omega_2)] \langle a_1^\dagger a_2 a_2^\dagger a_1 \rangle. \end{aligned} \quad (5)$$

The third-order material susceptibility functions are as follows:

$$\chi^{(vi)}(\omega_1, \omega_2) = (-1)/3! \sum_e \sum_{g'} \sum_{e'} \mu_{g_1 e'}^\beta \mu_{e' g'}^\alpha \mu_{g' e}^\alpha \mu(e g_1)^\beta g_{e g_1}(\omega_2) g_{g' g_1}(\omega_2 - \omega_1) g_{e' g_1}(\omega_2), \quad (6)$$

$$\chi^{(viii)}(\omega_1, \omega_2) = (-1)/3! \sum_e \sum_{g'} \sum_{e'} \mu_{g_1 e'}^\alpha \mu_{e' g'}^\beta \mu_{g' e}^\beta \mu_{e g_1}^\alpha g_{e g_1}(\omega_1) g_{g' g_1}^*(\omega_1 - \omega_2) g_{e' g_1}^*(\omega_1). \quad (7)$$

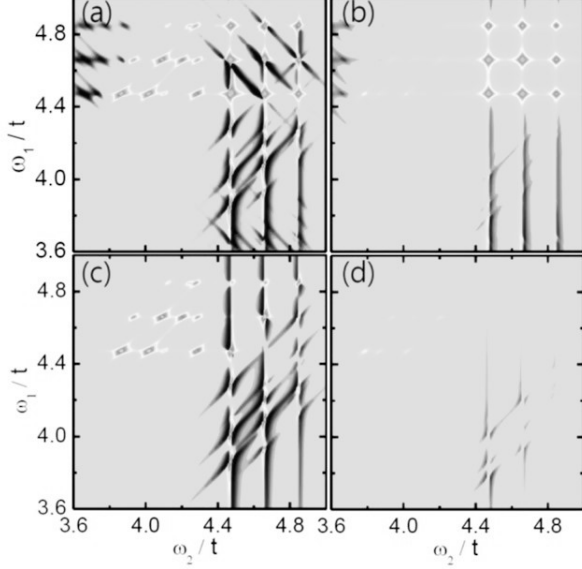


FIG. 2: (a, b) Conventional excitation-probe signals for (a) the parallel polarization and (b) the perpendicular polarization. (c, d) Excitation probe signals obtained with the proposed method for (c) the parallel polarization and (d) the perpendicular polarization.

Here, $\mu_{eg}^{\alpha,\beta}$ is the dipole matrix element between the two energy eigenstates $|e\rangle$ and $|g\rangle$ of the full Hamiltonian (H), namely, $\langle e|r|g\rangle$; r is the dipole displacement operator. The superscripts α and β indicate the polarization directions of the a_1 (excitation) and a_2 (probe) fields, respectively. $g_{eg}(\omega)$ is the auxiliary function representing the Lorentzian response[9]:

$$g_{eg}(\omega) = 1/(\omega - (E_e - E_g) + I\gamma). \quad (8)$$

Here, E_g (E_e) is the energy eigenvalue of $|g\rangle$ ($|e\rangle$), and γ is the spectral broadening parameter. A phenomenological value ($0.05t$) was used for γ to obtain the results shown in Figs. 2, 3, 5, and 6.

III. RESULTS & DISCUSSION

First we calculated the conventional excitation-probe signal. For parallel polarizations of the excitation pulse and probe pulse, numerous peaks were observed, arising from the superposition of the TPA and SRS processes contributed by all eight pathways

(Fig. 2a). Figure 2b shows the perpendicular polarization case.

Next we applied the proposed method. Figure 2c shows the excitation-probe signal for the parallel polarization case. Spectral structures arising from TPA contributions and some of the SRS contributions shown in Fig. 2a do not appear in Fig. 2c. For example, the structures between $\omega_1 = 4.5t$ and $\omega_1 = 4.9t$ and between $\omega_2 = 3.6t$ and $\omega_2 = 3.8t$ which arise from the TPA contributions, are not present in Fig. 2c.

Figure 2c shows two peaks along the diagonal line at $\omega_1 = \omega_2 = 4.45t$ and at $\omega_1 = \omega_2 = 4.65t$. The $\omega_1 = 4.45t$ peak arose from the $g_1 \rightarrow e_1 \rightarrow g_1 \rightarrow e_1 \rightarrow g_1$ transition process, and the $\omega_1 = 4.65t$ peak arose from the $g_1 \rightarrow e_2 \rightarrow g_1 \rightarrow e_2 \rightarrow g_1$ process. In addition to these peaks, more peaks appeared along the vertical line at $\omega_2 = 4.45t$ and at $\omega_2 = 4.65t$, owing to the contribution of the (vi) pathway. Peaks appeared along the horizontal line at $\omega_1 = 4.45t$ and at $\omega_1 = 4.65t$ owing to the contribution of the (viii) pathway. Figure 2d shows the perpendicular polarization case. Note that the $g_1 \rightarrow e_1 \rightarrow g_1 \rightarrow e_1 \rightarrow g_1$ transition peak is clearer than the other peaks. In an experiment, Figs. 2c and 2d can be obtained by measuring the spectral transmittance of the probe signal, because $S(\omega_1, \omega_2)$ is proportional to the transmittance intensity change.

We found an additional advantage of the proposed method. The excitation-probe signals shown in Figs. 3e and 3f are the products of the susceptibility function (Figs. 3a and 3b) and the photon correlation function (Figs. 3c and 3d) as described in Eq. (5). The proposed method allows tuning of the spectral widths and positions of the photon correlation functions. This tunability can help to enhance the excitation-probe signal of some specific group of transitions and to suppress the other signals selectively.

We controlled the spectral distribution of the photon correlation function by changing a parameter of the joint distribution function, $|\Phi_{ij}|^2$. Figure 4 shows the two cases of $|\Phi_{ij}|^2$; the $|\Phi_{ij}|^2$ shown in Fig. 4a corresponds to the photons of Figs. 3c and 3d. Here, the parameters ω_p , T_1 , and T_2 were $8.94t$, $31.0/t$, and $0.1/t$. The $|\Phi_{ij}|^2$ shown in Fig. 4b corresponds to the photons of Figs. 5a and 5b. Here, the parameters ω_p and T_1 were same; only T_2 was differ-

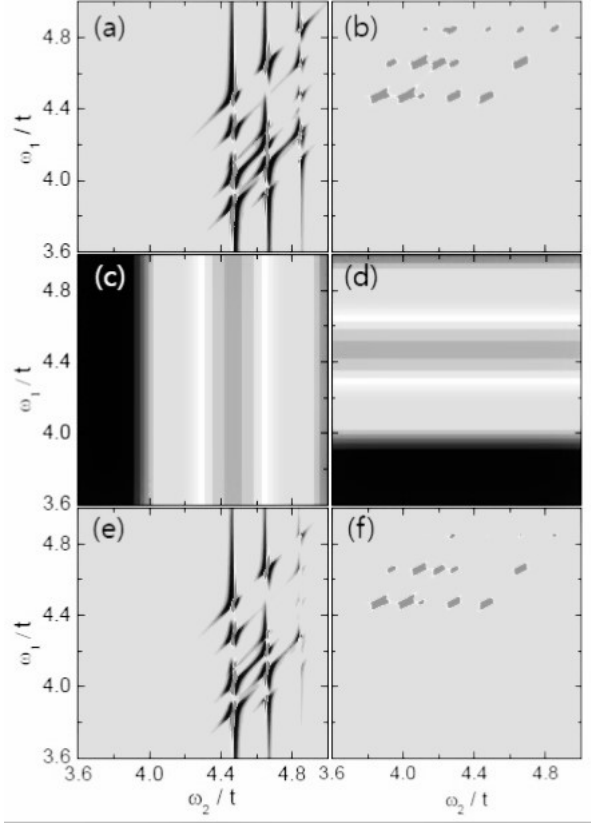


FIG. 3: (a, b) Susceptibility functions for (a) the (vi) pathway ($Im[\chi^{(vi)}(\omega_1, \omega_2)]$) and (b) the (viii) pathway ($Im[\chi^{(viii)}(\omega_1, \omega_2)]$). (c, d) Photon correlation functions for (c) the (vi) pathway ($\langle a_2^\dagger a_1 a_1^\dagger a_2 \rangle$) and (d) the (viii) pathway ($\langle a_1^\dagger a_2 a_2^\dagger a_1 \rangle$). (e, f) Excitation-probe signals for (e) the (vi) pathway ($S^{(vi)}(\omega_1, \omega_2)$) and (f) the (viii) pathway ($S^{(viii)}(\omega_1, \omega_2)$).

ent ($T_2 = 0.3/t$). T_2 can be controlled by changing the thickness of the nonlinear crystal[11]. Figures 5a and 5b show the photon correlation functions with longer T_2 (i.e. with narrower bandwidth) than those in Figs. 3c and 3d; Fig. 5a shows the photon correlation function for the (vi) pathway and Fig. 5b shows the function for the (viii) pathway. Figures 5c and 5d show the excitation-probe signal produced by the narrow-bandwidth photon correlation functions; compared with Figs. 3e and 3f, the SRS peaks arising from the $g_1 \rightarrow e_1 \rightarrow g_4 \rightarrow e_1 \rightarrow g_1$ transition remain clear whereas the other peaks are diminished.

We found that the polarization states of pulses reveal the rotational symmetry of the excitations. Figures 6a and 6b present the SRS signal due to the quasiparticle (phonon and phonon-coupled orbiton) excitations in the model material system, LaMnO₃. Figure 6a shows the signal of the parallel polarization state; the peaks arise from the $g_1 \rightarrow e_1 \rightarrow g_n \rightarrow e_1 \rightarrow g_1$ transition pathways. Here we only focus on the peaks above the diagonal ($\omega_1 = \omega_2$) line. Peaks

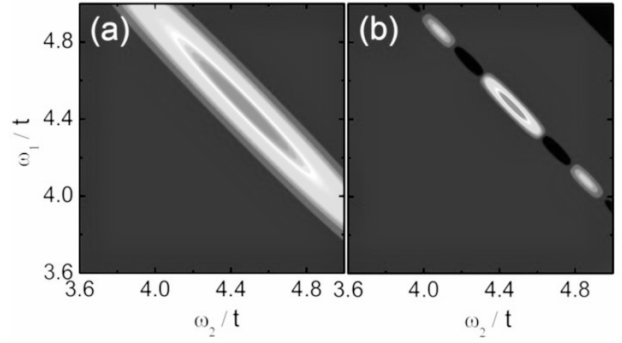


FIG. 4: Joint spectral density functions for different photon pair entanglement times (T_2): (a) $T_2 = 0.1/t$, (b) $T_2 = 0.3/t$.

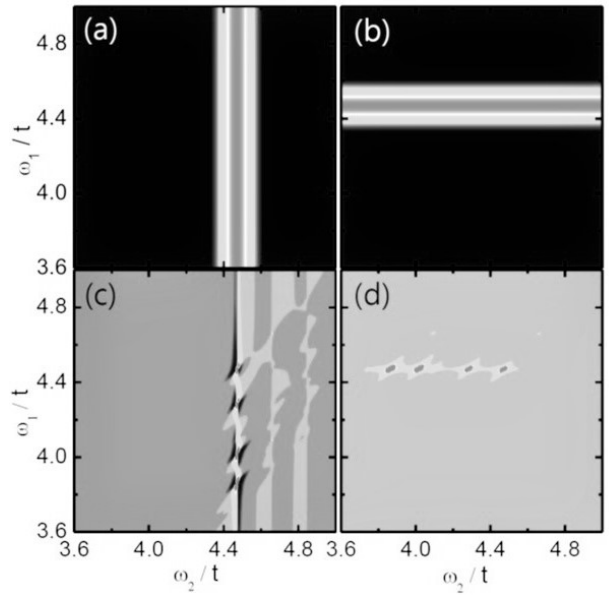


FIG. 5: (a, b) Photon correlation functions for (a) the (vi) pathway and (b) the (viii) pathway. (c, d) SRS signals for (c) the (vi) pathway and (d) the (viii) pathway.

at lower parts can be understood similarly. When $n = 1$, the pathway corresponds to Rayleigh scattering, which results in the peak at $\omega_1 = \omega_2 = 4.45t$. When $n = 2$, the pathway corresponds to JahnTeller phonon excitation with A_g symmetry, which results in the peak at $(\omega_1 = 4.45t, \omega_2 = 4.3t)$. When $n = 3$ and 4, the pathways involve the orbital excitation. In particular, the $n = 4$ transition pathway results in the so-called phonon-coupled orbiton, which results in the peak at $(\omega_1 = 4.45t, \omega_2 = 3.85t)$ [14]. The strength of the peaks depends on the dipole matrix elements: $\mu(g_1 e_1)^\beta \mu(e_1 g_n)^\alpha \mu(g_n e_1)^\alpha \mu(e_1 g_1)^\beta$, as described in Eq.(6). Figure 6b shows the perpendicular polarization case; i.e. $\alpha \perp \beta$. Because of the broken rotational symmetry of the excited orbitals in

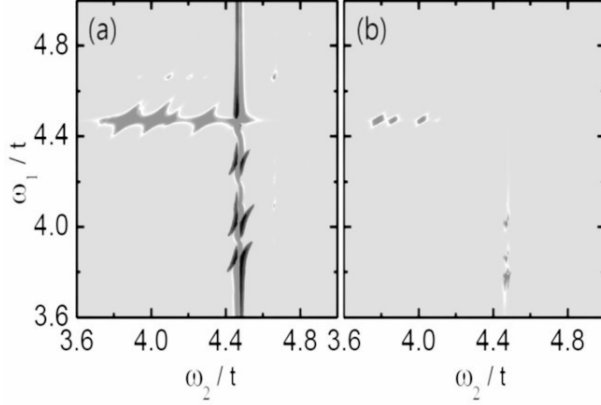


FIG. 6: Excitation probe signals simulated with narrower-bandwidth photon correlation functions ($T_2 = 0.3/t$ case) for (a) parallel polarization and (b) perpendicular polarization of the excitation and probe pulses.

$|g_3\rangle$ and $|g_4\rangle$, $\mu(g_1 e_1)^\beta \mu(e_1 g_n)^\alpha \mu(g_n e_1)^\alpha \mu(e_1 g_1)^\beta$ remains finite for the pathways involving the orbital excitation (i.e. $g_1 \rightarrow e_1 \rightarrow (g_3, g_4) \rightarrow e_1 \rightarrow g_1$), whereas the matrix elements involving $|g_1\rangle$ and $|g_2\rangle$ become zero. Note that the peaks at $(\omega_1 = 4.45t, \omega_2 = 3.85t)$ remain whereas the other peaks are suppressed in Fig. 6b. The broken rotational symmetry of the intermediate state allows the intensity of the SRS signal to remain finite even in the perpendicular

polarization geometry of the excitation-probe pulses. Comparison of the SRS signals measured with different polarization configurations of the pulses can test the rotational symmetry of the excited states.

IV. CONCLUSIONS

We have proposed an excitation-probe method using entangled photon pulses. Numerical simulation demonstrated that the two-photon absorption signal can be selectively filtered in the excitation-probe signal. By controlling the crystal thickness and the pump pulse frequency for the parametric downconversion, we can tune the bandwidth and the central frequency of the photon correlation function distribution used in the proposed method. It can be found that this tuning can be used to select specific transition peaks from the group of numerous stimulated Raman scattering peaks. We demonstrated that the proposed method can be used to examine the stimulated Raman scattering signal arising from orbital wave excitation in a model material, LaMnO₃.

Acknowledgments

This research was supported by the National Research Foundation of Mongolia (Grants No. SSA_017/2016).

V. APPENDIX

A. Photon correlation function

The photon correlation functions for some pathways are zero. Following is the proof for one of those pathways:

$$\langle a_{1i}^\dagger a_{2j}^\dagger a_{2j} a_{1i} \rangle = 1/4 \langle (-Ib_{2i}^\dagger - b_{1i}^\dagger)(-Ib_{1j}^\dagger - b_{2j}^\dagger)(Ib_{1j} - b_{2j})(Ib_{2i} - b_{1i}) \rangle; \quad (9)$$

for the ket side,

$$(Ib_{1j} - b_{2j})(Ib_{2i} - b_{1i})|\Psi\rangle = \sum_{k,l} \Phi_{kl}(b_{2j}b_{1i} - b_{2i}b_{1j})b_{1k}^\dagger b_{2l}^\dagger|0\rangle = \Phi_{ij}|0\rangle - \Phi_{ji}|0\rangle = 0. \quad (10)$$

Note here that $\Phi_{ij} = \Phi_{ji}$ for a type-I nonlinear crystal. Therefore,

$$\langle a_{1i}^\dagger a_{2j}^\dagger a_{2j} a_{1i} \rangle = 0. \quad (11)$$

The photon correlation functions for the (vi) and (viii) pathways shown in Fig.1c can be expressed as follows:

$$\langle a_{1i}^\dagger a_{2j}^\dagger a_{2j} a_{1i} \rangle = \langle a_{1i}^\dagger a_{1i} \rangle + \langle a_{1i}^\dagger a_{2j}^\dagger a_{2j} a_{1i} \rangle. \quad (12)$$

The second term on the right side is zero. The first term is

$$\begin{aligned} \langle \Psi|a_{1i}^\dagger a_{1i}|\Psi\rangle &= \sum_{m,n} \sum_{k,l} \langle 0|\Phi_{mn}^* \Phi_{kl} b_{1m} b_{2n} a_{1i}^\dagger a_{1i} b_{1k}^\dagger b_{2l}^\dagger|0\rangle \\ &= 1/2 \sum_{m,n} \sum_{k,l} \langle 0|\Phi_{mn}^* \Phi_{kl} b_{1m} b_{2n} (-Ib_{2i}^\dagger - b_{1i}^\dagger)(Ib_{2i} - b_{1i}) b_{1k}^\dagger b_{2l}^\dagger|0\rangle = 1/2 \sum_j (|\Phi_{ij}|^2 + |\Phi_{ji}|^2). \end{aligned} \quad (13)$$

Similarly, $\langle a_{2i}^\dagger a_{1j} a_{1j}^\dagger a_{2i} \rangle = \langle a_{2i}^\dagger a_{2i} \rangle = \langle a_{1i}^\dagger a_{1i} \rangle$.

B. Two-photon absorption signal with frequency-correlated photons

One may wonder whether the quantum mechanical entanglement between the photons is necessary for the suppression of the two-photon absorption signal or whether similar results could be achieved by using frequency-correlated photons that are not entangled. To investigate this, we explore the case in which the two photons are frequency-correlated but nonetheless unentangled. To compute the photon correlation function, we can consider a classically correlated two-photon state described by a density operator of the following form[15]:

$$\rho = C \sum_{i,j} [\Phi_{ij}]^2 b_{1i}^\dagger b_{2j}^\dagger |0\rangle \langle 0| b_{1i} b_{2j}, \quad (14)$$

where $|\Phi_{ij}|^2$ is the joined distribution function of the photons and C is a normalization constant. Annihilation (creation) operators of these fields are represented by $b_1(b_1^\dagger)$ and $b_2(b_2^\dagger)$. Using this density operator, we can calculate two-photon correlation functions in group A. For example,

$$\langle b_{2k}^\dagger b_{1l}^\dagger b_{2k} b_{1l} \rangle = \text{Tr}[b_{2k} b_{1l} b_{2k}^\dagger b_{1l}^\dagger] = C \sum_{i,j} |\Phi_{ij}|^2 \text{Tr}[b_{2k} b_{1l} b_{1i}^\dagger b_{2j}^\dagger |0\rangle \langle 0| b_{1i} b_{2j} b_{2k}^\dagger b_{1l}^\dagger] = C |\Phi_{lk}|^2. \quad (15)$$

All of the correlation functions are identical and nonzero, which means that we cannot suppress the TPA signal using the frequency-correlated, unentangled photons.

-
- [1] D. N. Basov, R. D. Averitt, D. V. Marel, M. Dressel, and K. Haule, *Rev. Mod. Phys.* **83**, 471 (2011).
 - [2] T. E. Stevens, J. Kuhl, and R. Merlin, *Phys. Rev. B* **65**, 144304 (2002).
 - [3] C. A. Marx, U. Harbola, and S. Mukamel, *Phys. Rev. A* **77**, 022110 (2008).
 - [4] A. M. Weiner, D. E. Leaird, G. P. Weiderrecht, and K. A. Nelson, *J. Opt. Soc. Am. B* **8**, 061264 (1991).
 - [5] D. Zhang, M. N. Slipchenko, D. E. Leaird, A. M. Weiner, and J.-X. Cheng, *Opt. Exp.* **21**, 13864 (2013).
 - [6] R. Glenn and M. Dantus, *J. Phys. Chem. Lett.* **7**, 117 (2016).
 - [7] K. Isobe, H. Kawano, A. Suda, A. Kumagai, A. Miyawaki, and K. Midorikawa, *K. Biomed. Opt. Ex.* **4**, 1548 (2013).
 - [8] F. E. Robles, J. W. Wilson, M. C. Fischer, and W. S. Warren, *Opt. Ex.* **20**, 17082 (2012).
 - [9] O. Roslyak, C. Marx and S. Mukamel, *Phys. Rev. A* **79**, 033832 (2009).
 - [10] O. Roslyak, and S. Mukamel, *Phys. Rev. A* **79**, 063409 (2009).
 - [11] W. P. Grice and I. A. Walmsley, *Phys. Rev. A* **56**, 1627 (1997).
 - [12] The phase matching condition was considered inside the nonlinear crystal. In free space the magnitude and the direction of the wave-vectors can be different because of the refraction.
 - [13] E. M. Nagasako, S. J. Bentley, R. W. Boyd, and G. S. Agarwal, *Phys. Rev. A* **64**, 043802 (2001).
 - [14] P. Munkhbaatar, and K. Myung-Whun, *J. Mod. Opt.* **61**, 197 (2014).
 - [15] R. de J. Len-Montiel et al, *New J. Phys.* **15**, 053023 (2013).